

MEDUSA: Minkowski functionals estimated from Delaunay tessellations of the three-dimensional large-scale structure

Martha Lippich[★] and Ariel G. Sánchez

Max-Planck-Institut für extraterrestrische Physik, Postfach 1312, Giessenbachstr., 85741 Garching, Germany

Submitted to MNRAS

ABSTRACT

Minkowski functionals (MFs) are a set of statistics that characterise the geometry and topology of the cosmic density field and contain complementary information to the standard two-point analyses. We present MEDUSA, an implementation of an accurate method for estimating the MFs of three-dimensional point distributions. These estimates are inferred from triangulated isodensity surfaces that are constructed from the Delaunay tessellation of the input point sample. Contrary to previous methods, MEDUSA can account for periodic boundary conditions, which is crucial for the analysis of N -body simulations. We validate our code against several test samples with known MFs, including Gaussian random fields with a Λ CDM power spectrum, and find excellent agreement with the theory predictions. We use MEDUSA to measure the MFs of synthetic galaxy catalogues constructed from N -body simulations. Our results show clearly non-Gaussian signatures that arise from the non-linear gravitational evolution of the density field. We find that, although redshift-space distortions significantly change our MFs estimates, their impact is considerably reduced if these measurements are expressed as a function of the volume-filling fraction. We also show that the effect of Alcock-Paczynski (AP) distortions on the MFs can be described by scaling them with different powers of the isotropic AP parameter q defined in terms of the volume-averaged distance $D_V(z)$. Thus the MFs estimates by MEDUSA are useful probes of non-linearities in the density field, and the expansion and growth of structure histories of the Universe.

Key words: methods: statistical – large-scale structure of Universe

1 INTRODUCTION

The analysis of the large-scale distribution of galaxies by means of two-point statistics, such as the correlation function or the power spectrum, has played a key role in establishing the current Λ CDM cosmological paradigm (Davis & Peebles 1983; Efstathiou et al. 2002; Tegmark et al. 2004; Cole et al. 2005; Eisenstein et al. 2005; Blake et al. 2011; Sánchez et al. 2006, 2017; Alam et al. 2017a; eBOSS Collaboration et al. 2020). However, as the late time matter density field is not simply Gaussian distributed, two-point statistics cannot provide a complete description of the large-scale structure (LSS) of the Universe. Extending current cosmological analyses to higher order statistics is essential to exploit the full potential of upcoming high-precision surveys such as the dark energy spectroscopic instrument (DESI, DESI Collaboration et al. 2016), and the ESA space mission *Euclid* (Laureijs et al. 2011).

A full characterization of the density field would require measuring an infinite hierarchy of N -point correlation functions. Present-day surveys allow for accurate measurements of the three-point correlation function and the bispectrum (Marín et al. 2013; Gil-Marín et al. 2015; Gil-Marín et al. 2017; Slepian et al. 2017a,b;

Pearson & Samushia 2018). These analyses are challenging due to the complexity associated with the measurement of all possible combinations of triplets, their corresponding theoretical modelling, and the estimation of accurate covariance matrices. The analysis of higher order N -point functions is at the moment infeasible.

Additional statistics that encode compressed higher-order information have been proposed as alternatives to complement the standard two-point analyses. Among others, these include measurements of count in cells (e.g. de Lapparent et al. 1991; Peebles 1993; Repp & Szapudi 2020; Uhlemann et al. 2020), the void probability function (e.g. White 1979; Perez et al. 2020), and the genus (e.g. Gott et al. 1986; Weinberg et al. 1987; Appleby et al. 2020). In this work, we focus on the full set of Minkowski functionals (MFs), introduced to LSS studies by Mecke et al. (1994) to describe the geometry and topology of the cosmic density field. In three dimensions, there are four MFs: surface area, volume, curvature and the Euler characteristic (or the genus). For Gaussian density fields, the MFs of isodensity surfaces follow known analytical predictions that are sensitive to the power spectrum of the sample (Tomita 1990; Schmalzing & Buchert 1997; Matsubara 2003). The non-linear gravitational evolution of the density field leads to deviations from Gaussianity, which manifest most notably in the asymmetry of the genus curve (Matsubara 1994), but also affect the other MFs. New theoretical predictions for

[★] E-mail: mlippich@mpe.mpg.de

the MFs of weakly non-Gaussian fields (Pogosyan et al. 2009; Matsubara 2010; Gay et al. 2012; Matsubara & Kuriki 2020; Matsubara et al. 2020), even accounting for redshift-space distortions (RSD) (Codis et al. 2013), make it possible to access further information encompassing higher-order correlations, as well as the growth-rate of cosmic structure. Additionally, other aspects of the evolution of density fluctuations can be explored using MFs, such as the subtle effect of massive neutrinos on the morphology of the LSS (Liu et al. 2020).

Although in this work we focus on the extraction of the MFs of the three-dimensional galaxy density field, there are several additional applications of these statistics in cosmological data analyses. Two-dimensional MFs have been extensively used to analyse non-Gaussianities in the CMB (e.g. Schmalzing & Gorski 1998; Hikage et al. 2006; Buchert et al. 2017; Planck Collaboration et al. 2020). Weak lensing shear fields and convergence maps have also been investigated by means of MFs (e.g. Petri et al. 2013; Spurio Mancini et al. 2018; Munshi et al. 2020; Parroni et al. 2020). Other fields of application are 21 cm and reionization studies, for which MFs represent useful morphological descriptors (e.g. Wang et al. 2015; Yoshiura et al. 2017; Chen et al. 2019).

There are two main approaches to estimate MFs of the three-dimensional galaxy distribution. One method is to use germ-grain models that construct the MFs from intersecting spheres inflated around the input point sample (see, e.g., Mecke et al. 1994; Schmalzing et al. 1996; Kerscher 2000, for a comprehensive overview). The most useful aspect of this approach is that the resulting MFs can be directly expressed as sums over integrals of the N -point correlation functions (Schmalzing et al. 1999a; Wiegand et al. 2014). The other popular approach is to estimate isodensity MFs, which are measured in terms of excursion sets. Isodensity MFs are more directly linked to the underlying density field than the ones from germ-grain models, and have the advantage that they can be modelled with the previously mentioned theory predictions. Different methods to compute isodensity MFs from a galaxy distribution have been proposed, the most common ones are Koenderink invariants from differential geometry and Crofton’s intersection formula from integral geometry (Schmalzing & Buchert 1997; Schmalzing et al. 1999b).

MFs have been used to analyse LSS data for almost three decades, leading to interesting cosmological results. The germ-grain MFs have been used to study several galaxy and galaxy cluster catalogues (e.g. Mecke et al. 1994; Kerscher et al. 1997, 1998, 2001; Wiegand et al. 2014). The recent work of Wiegand & Eisenstein (2017) studied the germ-grain MFs of the northern CMASS galaxy sample of SDSS BOSS DR12 and showed that they include contributions up to the sixth-point correlation function. Isodensity MFs have also been measured from LSS observations. Most analyses focused on the genus statistic only (e.g. Park et al. 2005; Gott et al. 2009; James et al. 2009; Choi et al. 2010; Zhang et al. 2010). Measurements of the four MFs based on Crofton’s formula have been obtained from a preliminary SDSS sample by Hikage et al. (2003) and the WiggleZ Dark Energy Survey (Drinkwater et al. 2010) by Blake et al. (2014).

An alternative approach for the estimation of isodensity MFs is to compute these statistics on triangulated isodensity surfaces constructed from the underlying density field. Although this approach follows very closely the geometry of the isodensity surfaces, it has so far received little attention. Sheth et al. (2003) developed a code to construct triangulated surfaces from fixed lattice cubes and Sheth (2004) used it to analyse N -body simulations with different cosmologies. Yaryura et al. (2004) and Aragon-Calvo et al. (2010)

proposed to define the triangulated surface directly from a Delaunay tessellation of the galaxy distribution instead of using a regular grid.

This paper presents a new implementation of an algorithm to construct triangulated isodensity surfaces based on the Delaunay tessellation and to estimate their corresponding MFs. Our code, MEDUSA, correctly accounts for periodic boundary conditions, which is crucial for the analysis of density fields from N -body simulations and the correct comparison of the measurements against theory predictions. After validating MEDUSA thoroughly using a series of test samples for which the MFs can be theoretically predicted, we apply it to the analysis of synthetic galaxy catalogues based on the Minerva simulations (Grieb et al. 2016; Lippich et al. 2019). We focus on three main issues of great importance for the analysis of the MFs of triangulated surfaces inferred from real galaxy surveys: non-Gaussian features due to non-linear gravitational evolution, redshift-space distortions (RSD), and Alcock-Paczynski (AP) distortions.

Our paper is structured as follows. In Section 2 we give a brief overview of MFs and describe the basic algorithm to measure them implemented in MEDUSA. In Section 3 we test MEDUSA by applying it to samples with known theoretical predictions for their MFs, including spherical, ellipsoidal and toroidal density distributions, as well as a Gaussian density field. In Section 4 we discuss how we reconstruct the underlying density field from discrete point samples. In Section 5 we apply MEDUSA to the Minerva HOD galaxy samples in real and redshift space, and assess the impact of AP distortions. We present our conclusions in Section 6.

2 EXTRACTING MINKOWSKI FUNCTIONALS FROM A DELAUNAY TESSELLATION

2.1 Minkowski Functionals

Minkowski Functionals (MFs) map the geometry and topology of an N -dimensional manifold into a set of $N + 1$ scalars. In our case, we consider as manifolds the excursion sets of the three-dimensional density field obtained by applying a given density threshold, ρ_{th} . Points for which $\rho(\mathbf{r}) > \rho_{\text{th}}$ are considered to be inside the isodensity surfaces. For this three-dimensional manifold there are four MFs:

- (i) the *surface area* S ,
- (ii) the *volume* V enclosed by the surface,
- (iii) the *integrated mean curvature* C of the surface,

$$C = \frac{1}{2} \oint_S \left(\frac{1}{R_1} + \frac{1}{R_2} \right) dS, \quad (1)$$

where R_1 and R_2 are the principal radii of curvature at a given point on the surface,

- (iv) the *integrated Gaussian curvature* of the surface,

$$\chi = \frac{1}{2\pi} \oint_S \left(\frac{1}{R_1 R_2} \right) dS, \quad (2)$$

also known as *Euler-characteristic*.

As can be seen from these equations, the MFs provide direct information about the geometry of the isodensity surface. In addition, the Euler characteristic also contains topological information, since it is related to the genus of the surface, $G = 1 - \chi/2$. The genus is a fundamental quantity in topology and corresponds to the number of holes of the surface, or more precisely

$$G = 1 + \text{number of holes} - \text{number of isolated regions},$$

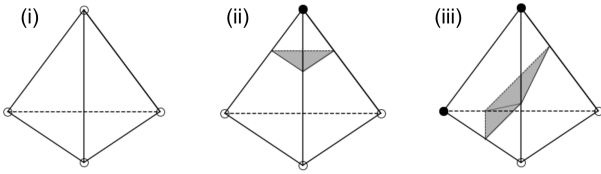


Figure 1. The three different tetrahedron configurations considered in MEDUSA: (i) all vertices are the same, either underdense or overdense compared to the density threshold ρ_{th} , here shown as empty circles, (ii) one vertex is different to the others, here shown as filled circle, (iii) two vertices are underdense and the other two are overdense. The different fillings of the circle indicate the different densities. The grey area shows the intersection of the triangulated isodensity surface with the tetrahedron.

where a hole is what is commonly referred to as tunnel in large-scale structure. For example, the genus of a sphere is $G = 0$, the genus of a torus with one handle is $G = 1$ and the genus of an eyeglasses frame is $G = 2$. Closed multiply-connected surfaces always have $G > 0$. Furthermore, the MFs have some mathematical properties that are useful for large-scale structure analyses, in particular that they are additive and translational invariant.

It is common to work in terms of Minkowski functional densities, which are obtained by rescaling the global MFs by the total volume considered, V_{tot} . The rescaled volume functional is often referred to as the volume-filling fraction

$$f_V = V/V_{\text{tot}}. \quad (3)$$

We will denote the surface, curvature, and genus densities by s , c , and g , respectively.

2.2 The MEDUSA code

In real or synthetic galaxy catalogues in general we do not know the underlying continuous density field. Instead, we have to estimate the isodensity MFs from a discrete three-dimensional point distribution. For this, we need three main ingredients

- (i) an estimate of the density at each point of the distribution,
- (ii) a fast and accurate extraction of the isodensity surfaces based on the point distribution for any given density threshold,
- (iii) the computation of the MFs of the resulting isodensity surface.

These three steps are implemented into our code MEDUSA (Minkowski functionals Estimated from DelaUnay tessellation). There are several approaches to estimate densities based on a discrete set of points. However, the second and third steps only require a set of points with known densities as an input and are independent of the particular method used to obtain such values. In the following two subsections, we describe each of the two steps (ii) and (iii) in detail and come to point (i) in Section 4 after testing MEDUSA extensively on point distributions with known densities.

2.2.1 Extraction of isodensity surfaces

The crucial step for the estimation of the MFs is the extraction of the isodensity surfaces at a desired threshold from a set of points. For MEDUSA we chose a similar approach to Sheth et al. (2003), Yaryura et al. (2004) and Aragon-Calvo et al. (2010), and compute a triangulated isodensity surface directly from a three-dimensional point distribution. We extend these previous approaches by also including a recipe to account for periodic boundary conditions.

Analogously to Yaryura et al. (2004) and Aragon-Calvo et al. (2010), we perform a Delaunay tessellation on the three-dimensional point distribution, which we use as the basis for the interpolation of the density field. This approach is simpler than the regular grid used by Sheth et al. (2003) and automatically provides us with higher resolution in the regions where the density is higher. In the case of point distributions from boxes with periodic boundary conditions, we add buffer zones around the box that replicate the particles from the opposite sides. MEDUSA assigns a flag to each tetrahedron resulting from the Delaunay tessellation. This flag depends on how many particles of the tetrahedron are inside the box and, if the tetrahedron lies (partially) outside the box, on its position. The following cases need to be considered:

- (i) Tetrahedra that lie completely inside the box.
- (ii) Tetrahedra that are partially outside the box and cross one face of the box far from its edges. Each of these tetrahedra has one copy at the opposite side of the box.
- (iii) Tetrahedra that are partially outside and lie close to the edges, but far from the corners of the box. Each of these tetrahedra has three copies at the three opposite edges of the box.
- (iv) Tetrahedra which are partially outside and lie close to the corners of the box. Each of these tetrahedra has seven copies at the other seven corners of the box.
- (v) For tetrahedra that are located at the corners of the box there is the special case that the vertices of the tetrahedron are all outside, but the tetrahedron is still partially inside the box.
- (vi) Tetrahedra close to the edges or corners that lie completely outside the box and are copies of tetrahedra that are completely inside the box, but are neighbours of tetrahedra that are partially inside.
- (vii) Tetrahedra that are completely outside the box and do not belong to the previous case (vi). They are also copies of tetrahedra that are completely inside the box.

The tetrahedra that belong to the last category (vii) can be discarded. All other tetrahedra are assigned a flag that takes into account to which category they belong and at which side of the box they are located, in order to prevent double counting. These flags are used in the estimation of the MFs as described in Section 2.2.2.

Additionally, all particles are considered as ‘‘overdense’’ or ‘‘underdense’’ depending on whether their corresponding densities are larger than the density threshold ρ_{th} being considered or not. Given this classification, there are only three different types of tetrahedron configurations:

- (i) All vertices of the tetrahedron are either overdense or underdense.
- (ii) One vertex is different to the other three vertices.
- (iii) Two vertices are overdense and the other two are underdense.

These three cases are illustrated in Fig. 1, where vertices with the same density property, i.e. underdense or overdense, are shown with circles with the same filling. The isodensity surface will only intersect tetrahedra of the last two types. This intersection will occur at the edges between particles with different density properties. The intersection points of the surface with the tetrahedron edges correspond to the points where the density matches the threshold ρ_{th} , which are obtained by linearly interpolating the densities of the two corresponding particles. This is equivalent to assuming a constant density gradient within the tetrahedron. For case (ii), where one particle is different to the others, we obtain an intersection triangle. For case (iii), where two particles have the same density property, we obtain four points of intersection on the edges and the

resulting surface can be decomposed into two triangles. Following this approach, MEDUSA computes the intersection triangles for all tetrahedra where at least one vertex is different to the others. These are 12 configurations less to take into account than for cubic lattice intersections as in [Sheth et al. \(2003\)](#), which makes this step significantly simpler. Once all tetrahedra of types (ii) and (iii) have been considered, we obtain a triangulated surface representing the isodensity contour corresponding to ρ_{th} .

2.2.2 Minkowski Functionals of a triangulated surface

Since the MFs are additive, the global MFs of the density distribution can be obtained by summing over the MFs of the isodensity surfaces enclosing the individual excursion sets. As described in [Sheth et al. \(2003\)](#), the MFs of a triangulated surface can be computed in a straightforward way:

(i) The surface area S of the triangulated surface is given by the sum over the areas of all triangles of the surface,

$$S = \sum_{i=1}^{N_t} S_i, \quad (4)$$

where N_t is the total number of triangles contributing to the surface.

(ii) The volume V is the sum over the volumes of all fully enclosed tetrahedra, denoted with T , and the fraction of the volumes of the intersected tetrahedra that lie within the surface, denoted with S ,

$$V = \sum_{i=1}^{N_T} V_i + \sum_{j=1}^{N_S} V_j. \quad (5)$$

If only one vertex is overdense or underdense, corresponding to case (ii) in [Fig. 1](#), the volume of the tetrahedron defined by this point and the triangle of the isodensity surface as a base has to be added or subtracted, respectively. If the tetrahedron contains two overdense vertices, as in case (iii) of [Fig. 1](#), the contributing volume can be split into three tetrahedra.

(iii) The integrated mean curvature C is obtained by summing over the edges of all adjacent triangles i and j ,

$$C = \frac{1}{2} \sum_{i,j} \ell_{ij} \phi_{ij} \epsilon \quad (6)$$

where ℓ_{ij} is the length of the common edge, ϕ_{ij} is the angle between the normals, \hat{n}_i and \hat{n}_j , of the two triangles,

$$\cos \phi_{ij} = \hat{n}_i \cdot \hat{n}_j, \quad (7)$$

and the value of ϵ distinguishes the cases in which the surface is locally convex, indicated by the value $\epsilon = 1$, or locally concave, in which case $\epsilon = -1$.

(iv) The Euler characteristic χ of a triangulated surface can be determined by

$$\chi = N_t - N_e + N_v, \quad (8)$$

where N_t , N_e and N_v are the total number of triangles, triangle edges and triangle vertices contained in the surface.

As mentioned in [Section 2.2.1](#), MEDUSA assigns a flag to every tetrahedron depending on its position in the box and/or the buffer zone. From the tetrahedra that are partially inside the box, and hence are repeated on its other sides, only those that are closer to the origin (0,0,0) are taken into account in the sums of equations (4)-(5), while all other copies are discarded. The flags that MEDUSA assigns

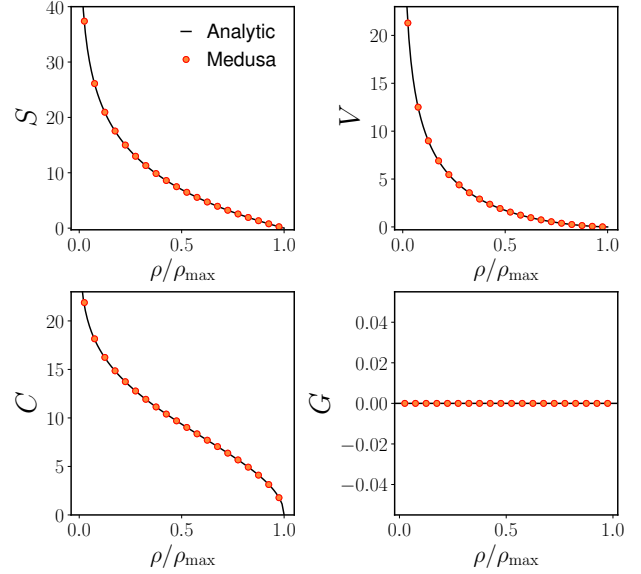


Figure 2. Minkowski Functionals inferred from a set of points following a spherically-symmetric Gaussian distribution as a function of the normalized density threshold ρ/ρ_{max} . The red circles correspond to the measurements from MEDUSA using 20 equispaced density thresholds, the black lines show the analytical predictions.

to each tetrahedron ensure that all triangle edges and vertices from tetrahedra that are partially inside the box are taken into account in the sums of equations (6)-(8), and that their contribution is counted only once.

3 RESULTS FOR TEST MODELS

In this section we test the performance of MEDUSA by measuring the MFs of point distributions following known density profiles.

3.1 Spherical density distribution

As a first test sample we consider a distribution of points following a spherically-symmetric Gaussian density profile given by

$$\rho(\mathbf{r}) = \rho_{\text{max}} \exp\left(-\frac{r^2}{2\sigma^2}\right), \quad (9)$$

where $r = |\mathbf{r}|$. We generated a set of points following this density profile with 3.5×10^5 particles, $\sigma = 0.6$ and a maximum radius, $r_{\text{max}} = 4.0$. The density at each point was obtained by evaluating the true density profile of equation (9) at the corresponding location. We used MEDUSA to measure the MFs of 20 equispaced density thresholds from $\rho/\rho_{\text{max}} = 0.0$ to 1.0. The analytical MFs for a sphere are:

- (i) $S(\rho_{\text{th}}) = 4\pi r(\rho_{\text{th}})^2$
- (ii) $V(\rho_{\text{th}}) = \frac{4}{3}\pi r(\rho_{\text{th}})^3$
- (iii) $C(\rho_{\text{th}}) = 4\pi r(\rho_{\text{th}})$
- (iv) $\chi(\rho_{\text{th}}) = 2$ and hence $G = 0$

The radius corresponding to a given density threshold, $r(\rho_{\text{th}})$, can

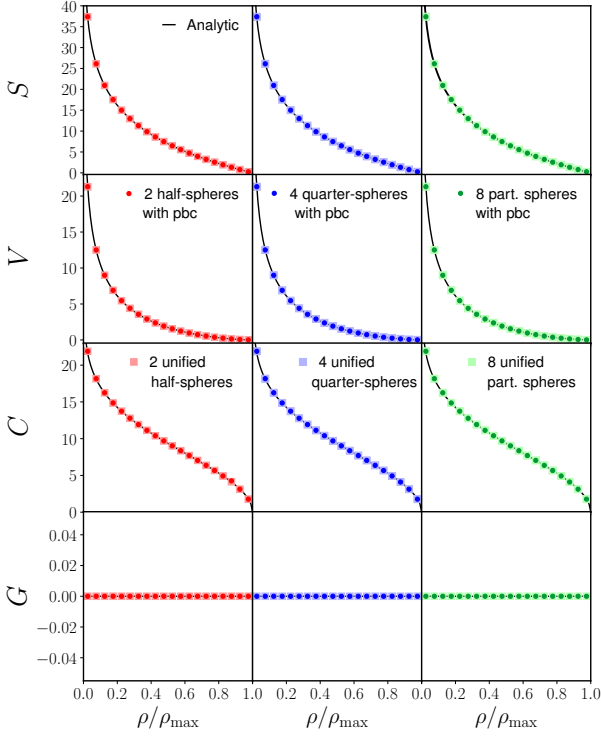


Figure 3. Minkowski Functionals of spherical density distributions where the spheres were cut into two half-spheres located at two opposite faces of a cubic box (red), four quarter-spheres located at the centres of four opposite edges of the box (blue), and eight partial spheres located at each corner of the box (green), measured with periodic boundary conditions. The measurements agree perfectly with the ones obtained from the corresponding unified spheres and their analytical predictions. All MFs are measured as a function of threshold ρ/ρ_{\max} .

be obtained by inverting equation (9). A lower density threshold corresponds to a larger radius of the spherical isodensity surface. Fig. 2 shows that the measured MFs are in good agreement with the analytical predictions. The overall agreement of the measurements of the first three MFs with the corresponding predictions is significantly better than 1%. The measured genus is always zero.

In order to test the implementation of periodic boundary conditions, we generated sets of points following the same spherically symmetric density profile of equation (9) but where the density distributions were cut into two half-spheres located at two opposite faces of a cubic box, four quarter-spheres located at the center of four opposite edges of the box, and eight partial spheres located at each corner of the box. Without the implementation of periodic boundary conditions, the isodensity surface cannot be extracted correctly at the boundaries of the box, since tetrahedra cannot extend outside it. Fig. 3 shows the agreement between the MFs measured from these three distributions taking into account periodic boundary conditions and the results obtained from the unified spherical distribution, for which no periodic boundary conditions are required. The agreement with the analytical predictions is also excellent. These results show that MEDUSA can correctly account for distributions with periodic boundary conditions. In particular, an error in the implementation of the periodic boundary conditions leading to a single incorrectly counted triangle, triangle vertex or triangle edge would result in values of genus $G \neq 0$.

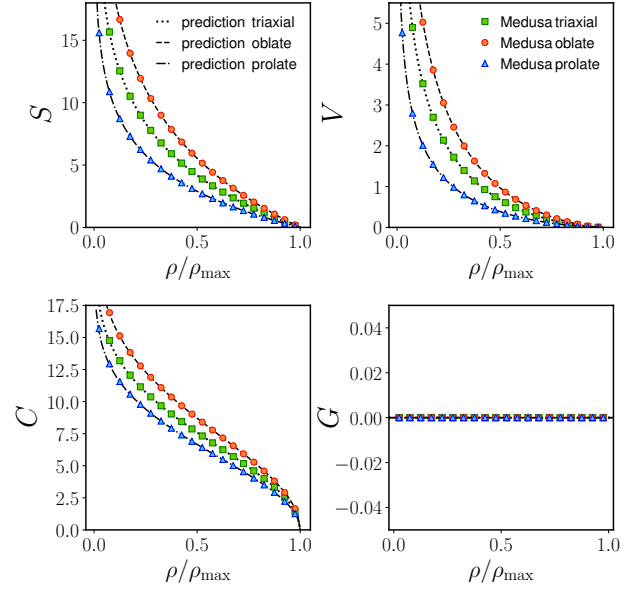


Figure 4. Minkowski Functionals for three different ellipsoidal point distributions, oblate, prolate, and triaxial, defined by the density profile of equation (10) expressed as a function of the normalized density ρ/ρ_{\max} . The lines indicate the corresponding theoretical predictions.

3.2 Ellipsoidal density distributions

We now consider as test samples ellipsoidal density distributions given by,

$$\rho(x, y, z) = \rho_{\max} \exp \left[- \left(\frac{x^2}{\sigma_a^2} + \frac{y^2}{\sigma_b^2} + \frac{z^2}{\sigma_c^2} \right) \right]. \quad (10)$$

We generated three different point distributions corresponding to oblate ($\sigma_a = \sigma_b = 1.0$, $\sigma_c = 0.4$), prolate ($\sigma_a = \sigma_b = 0.4$, $\sigma_c = 1.0$), and triaxial ($\sigma_a = 0.4$, $\sigma_b = 0.7$, $\sigma_c = 1.0$) ellipsoids using the same number of points and density thresholds as for the spherical case.

For the oblate and the prolate case, we compared the measured Minkowski functionals against analytical predictions. For the triaxial case no analytical predictions are known for the surface and the curvature and therefore we computed numerical predictions. As for the case of the spherical distributions, a lower density threshold corresponds to larger principal axes a, b, c of the ellipsoid, while conserving the constant axes ratios for all density thresholds, such that $b = a \frac{\sigma_b}{\sigma_a}$ and $c = a \frac{\sigma_c}{\sigma_a}$. The analytical predictions for the MFs are given by:

(i)

$$S_{\text{obl}} = 2\pi a (\rho_{\text{th}})^2 \left[1 + \frac{\sigma_c^2}{\sigma_a \sqrt{\sigma_a^2 - \sigma_c^2}} \operatorname{arctanh} \left(\sqrt{1 - \frac{\sigma_c^2}{\sigma_a^2}} \right) \right] \quad (11)$$

$$S_{\text{pro}} = 2\pi a (\rho_{\text{th}})^2 \left[1 + \frac{\sigma_c^2}{\sigma_a \sqrt{\sigma_c^2 - \sigma_a^2}} \operatorname{arcsin} \left(\sqrt{1 - \frac{\sigma_a^2}{\sigma_c^2}} \right) \right] \quad (12)$$

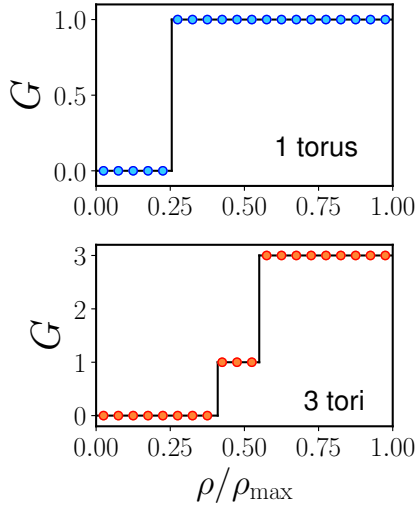


Figure 5. Genus measurements as a function of the normalized density ρ/ρ_{\max} of point distributions following profiles of one torus (upper panel) and three overlapping tori (lower panel). The solid lines show the theoretical predictions for each case.

(ii)

$$C_{\text{obl}} = 2\pi a(\rho_{\text{th}}) \left[\frac{\sigma_c}{\sigma_a} + \frac{\sigma_a}{\sqrt{\sigma_c^2 - \sigma_a^2}} \operatorname{arccosh} \left(\frac{\sigma_c}{\sigma_a} \right) \right] \quad (13)$$

$$C_{\text{pro}} = 2\pi a(\rho_{\text{th}}) \left[\frac{\sigma_c}{\sigma_a} + \frac{\sigma_a}{\sqrt{\sigma_a^2 - \sigma_c^2}} \operatorname{arccos} \left(\frac{\sigma_c}{\sigma_a} \right) \right] \quad (14)$$

(iii) $V = \frac{4}{3}\pi a(\rho_{\text{th}})^3 \frac{\sigma_b \sigma_c}{\sigma_a^2}$
 (iv) $\chi = 2$ and hence $G = 0$

Fig. 4 shows that in all cases the measured MFs agree perfectly with the theoretical predictions. As in the case for the spherical density distribution, the overall agreement of the measurements of the first three MFs with the corresponding predictions is better than 1%. The measured genus is always exactly zero.

3.3 Toroidal density profiles

The point distributions considered in the previous sections have isodensity surfaces without holes, and therefore their genus is zero for all density thresholds. In order to test the estimation of the Euler characteristic and the genus, we studied sets of points corresponding to one or more overlapping toroidal distributions. For the case of one torus, the point distribution is generated following a density profile

$$\rho(x, y, z) = \rho_{\max} \exp \left[-\frac{(R - \sqrt{x^2 + y^2})^2 + z^2}{\sigma^2} \right], \quad (15)$$

where R and r are the major and minor radii of the torus, respectively, and $r^2 = (R - \sqrt{x^2 + y^2})^2 + z^2$. The upper panel of Fig. 5 shows the measured genus of such a density distribution, generated with $R = 1.1$ and $\sigma = 0.9$. The upper panels of Fig. 6 show the corresponding triangulated isodensity surfaces obtained by MEDUSA for $\rho/\rho_{\max} = 0.225$, $\rho/\rho_{\max} = 0.475$ and $\rho/\rho_{\max} = 0.725$. For low

density thresholds, no hole is visible in the isodensity surface and MEDUSA measures $G = 0$. For density thresholds $\rho/\rho_{\max} > 0.25$ a hole in the center of the isodensity surface becomes visible and the code correctly recovers $G = 1$.

We also considered a set of points corresponding to three overlapping tori with $R = 1.3$ and $\sigma = 0.8$, and centred at $(1, 0, 0)$, $(-1, 0, 0)$ and $(0, 2, 0)$, respectively. The lower panel of Fig. 5 shows the genus measured from this density distribution, and the lower panels of Fig. 6 show three characteristic isodensity surfaces at the same thresholds as before. As in the case of a single torus, for low density thresholds the isodensity surface contains no holes and the measurement of the genus is $G = 0$. For a density threshold $0.4 < \rho/\rho_{\max} < 0.55$ the corresponding isodensity surface shows the hole of the torus whose center is furthest from the other two and hence the measured genus is $G = 1$. For a density threshold $\rho/\rho_{\max} > 0.55$, the isodensity surface contains three holes and we recovered the correct value $G = 3$.

3.4 Effect of using particles tracing the density field

When estimating MFs, MEDUSA uses the values of the density field directly at the positions of the points in the sample being analysed. In the test samples considered in the previous sections, as in numerical simulations or real galaxy surveys, the points trace the underlying density field. Using their positions as the nodes to interpolate the density field, as opposed to, e.g. the vertices of a regular grid, has the advantage of automatically providing a higher resolution in high-density regions. Note however, that the procedure described in Section 2.2 does not require the points used as the basis of the Delaunay tessellation to follow the density field. As a test, Fig. 7 shows the MFs for the same spherical density distribution as in Section 3.1 estimated using sets of particles of different size that are placed following the density distribution or randomly within the same volume. The computation of the genus is consistently zero for all considered cases and density thresholds. The remaining three MFs computed from the 100 000 and 350 000 particles tracing the density field agree with the analytical predictions at better than 1% level. Even for the case of 10 000 points the agreement between measurements and analytical predictions is better than 2% on densities $0.1 < \rho/\rho_{\max} < 0.8$. For the case of the randomly distributed particles, we obtain a comparable precision only when using 350 000 particles. For smaller samples, the deviations from the analytical predictions become significantly larger, particularly for high density thresholds. This comparison illustrates the advantage of using particles tracing the density field as the nodes of the Delaunay tessellation, which provides a better resolution on high-density regions and allows for a robust determination of all MFs even for sparse samples.

3.5 Gaussian density field

For a final test of MEDUSA, we computed the MFs of a smoothed Gaussian random field (GRF), which have known analytical expressions that are sensitive to the power spectrum of the field, $P(k)$. This case also serves as an additional validation of the implementation of periodic boundary conditions in our code, as an incorrect treatment would lead to deviations from the analytical predictions. We generated 100 realizations of a GRF with the same linear power spectrum as our Minerva simulations, which are described in Section 5 at redshift $z = 0.57$ on a cubic grid with side length $L = 737$ Mpc and periodic boundary conditions. The field, f , was smoothed with a

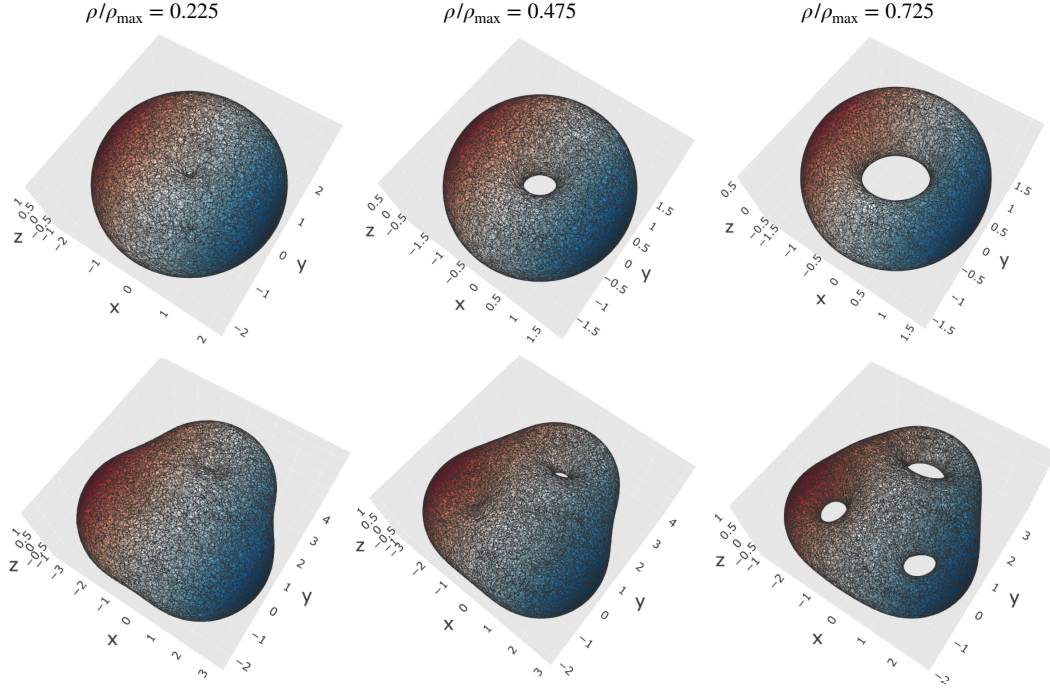


Figure 6. Isodensity surfaces for three different density thresholds $\rho/\rho_{\max} = 0.225$, $\rho/\rho_{\max} = 0.475$ and $\rho/\rho_{\max} = 0.725$ for density distributions following profiles of one torus (upper panel) and three overlapping tori (lower panel).

Gaussian kernel

$$W(x) = \frac{1}{(2\pi)^{3/2}R^3} \exp\left(-\frac{x^2}{2R^2}\right), \quad (16)$$

with a smoothing scale $R = 20$ grid units ($= 28.8$ Mpc) and normalized by its standard deviation, $v = f/\sigma_0$, such that it has zero mean, $\langle v \rangle = 0$, and unit variance, $\langle v^2 \rangle = 1$. Since there are grid cells with negative values of v , it cannot be treated as a density field and sampled with points. Instead, we follow the approach tested in Section 3.4 and use the values of v at 200 000 randomly placed points in each box. The resulting mean interparticle separation is approximately half of the smoothing length, and thus it should be possible to resolve the full structure of the smoothed density field.

The theoretical predictions for the MFs of a smoothed GRF only depend on the parameter λ_c , given by

$$\lambda_c = \sqrt{\frac{2\pi\xi(0)}{|\xi''(0)|}}, \quad (17)$$

which can be derived from the value of the correlation function $\xi(0)$ and its second derivative $\xi''(0)$ at zero separation. Both can be directly computed from the power spectrum of the sample as

$$\xi(0) = \langle f^2 \rangle = \sigma_0^2, \quad (18)$$

$$|\xi''(0)| = \langle |\nabla f|^2 \rangle = \sigma_1^2, \quad \text{and} \quad (19)$$

$$\sigma_j^2(R) = \int \frac{k^2 dk}{2\pi^2} k^{2j} P(k) \hat{W}(kR)^2, \quad (20)$$

in which $\hat{W}(kR)$ is the Fourier transform of the filter kernel of equation (16). For a GRF in three dimensions, the four MF densities are given by (Tomita 1990; Schmalzing & Buchert 1997; Matsubara

2003):

$$f_V(v) = \frac{1}{2} - \frac{1}{2}\Phi\left(\frac{v}{\sqrt{2}}\right), \quad (21)$$

where $\Phi(x) = \frac{2}{\sqrt{\pi}} \int_0^x dt \exp(-t^2)$ denotes the error function, (22)

$$s(v) = \frac{2}{\lambda_c} \sqrt{\frac{2}{\pi}} \exp\left(-\frac{v^2}{2}\right), \quad (23)$$

$$c(v) = \frac{\sqrt{2\pi}}{\lambda_c^2} v \exp\left(-\frac{v^2}{2}\right), \quad (24)$$

$$g(v) = \frac{1}{\lambda_c^3 \sqrt{2\pi}} (1 - v^2) \exp\left(-\frac{v^2}{2}\right). \quad (25)$$

From these expressions, it can be seen that the amplitudes of three of the MFs of a GRF are sensitive to its underlying power spectrum. Fig. 8 shows the mean MFs computed with MEDUSA from the 100 realizations of the GRF and their corresponding theoretical predictions, which are in good agreement. This shows that MEDUSA can accurately determine MFs of cosmological density fields and that the periodic boundary conditions are correctly implemented.

4 DENSITY ESTIMATION

The procedure to extract isodensity surfaces and estimate MFs described in Section 2.2 requires as input the values of the density at each point of our discrete distribution. In the test cases of Section 3, we used the true values of the underlying density field evaluated at the position of the points. When analysing N-body simulations or galaxy surveys, these densities need to be estimated from the

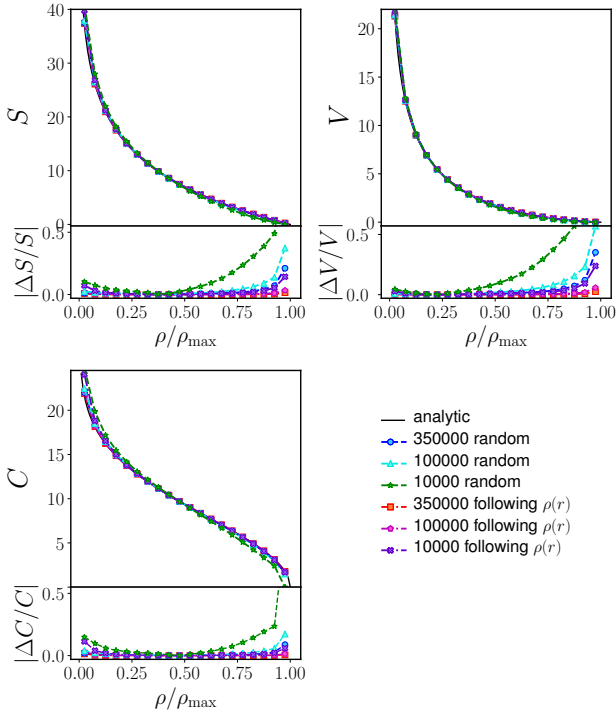


Figure 7. Minkowski Functionals for the spherical density distribution of Section 3.1 obtained using samples with 350 000, 100 000 and 10 000 points that are placed following the density profile or randomly within the same volume. The genus is not shown as it is consistently zero in all cases.

point distribution itself. Here, we estimate densities by applying a Gaussian kernel with a fixed smoothing scale λ ,

$$W(r) = \frac{1}{A} \exp\left(-\frac{r^2}{2\lambda^2}\right), \quad (26)$$

where r represents the distance between the points. This kernel is truncated at a scale r_{cut} and the normalization A is defined such that the volume integral of $W(r)$ up to this maximum scale is equal to one and hence the total mass is conserved. We tested this approach by applying it to the spherical Gaussian density distribution described in Section 3.1 for which the true underlying density distribution is known. We examined the impact of using different kernel smoothing lengths and truncation radii. The true underlying density profile corresponding to each case can be obtained by convolving the Gaussian density field of equation (9), which is truncated at $r_{\text{max}} = 4$, with the kernel of equation (26).

Fig. 9 shows the densities estimated at each point of the spherical Gaussian distribution of Section 3.1 by applying a Gaussian kernel with a smoothing length $\lambda = 0.2$ and a truncation radius of $r_{\text{cut}} = 2\lambda$, which follow closely the true profile, which is indicated by a black dashed line. Fig. 10 shows the MFs measured using these density estimates and the corresponding theory predictions computed using the convolved density profile. The measurements match the theory predictions remarkably well, with a similar level of agreement as for the case in which the true densities were used, which was discussed in Section 3.1. Note that, as the convolution with the Gaussian kernel reduces the maximum densities in the profile, the highest density threshold considered in this case is $\rho/\rho_{\text{max}} = 0.875$. We tested the impact of using different values of λ and r_{cut} and found similar results but with a larger variance.

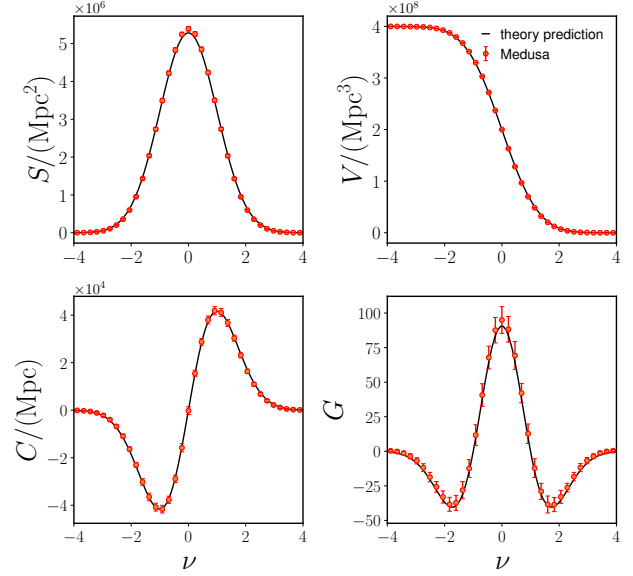


Figure 8. Mean MFs of 100 GRFs, generated with the same linear Λ CDM power spectrum as the Minerva simulations in a cubic box with length 737 Mpc and smoothed with a Gaussian kernel with $\lambda = 20$ grid units ($\lambda = 28.8$ Mpc). We used the densities at 200 000 random points within the box. The red points show the mean values determined using MEDUSA together with the standard deviation from 100 realizations. The theoretical predictions are shown as black solid lines.

When this method is applied to realistic point distributions such as galaxy catalogues, the smoothing length and truncation radius of the kernel need to be adjusted to provide the necessary smoothing to avoid discreteness effects without erasing too much information. In principle, steps (ii) and (iii) of the MEDUSA code described in Section 2.2 could be applied to density estimates obtained using a different approach. Other possibilities include non-parametric methods in which the densities are derived from the size of the Voronoi or Delaunay cells (e.g., Schaap & van de Weygaert 2000). Although these approaches can better resolve high-density regions due to their varying resolution, we have found that these density estimates are highly affected by Poisson noise in the low density regions of sparse samples, and are therefore not optimal for the analysis of real galaxy catalogues. An additional advantage of using an isotropic Gaussian kernel with a fixed smoothing length is that it is more convenient to compute theory predictions.

5 MINKOWSKI FUNCTIONALS OF THE MINERVA HOD GALAXY CATALOGUES

5.1 Real-space measurements

After validating the performance of MEDUSA for several test cases with different geometries and topologies, we now show the results obtained by applying the code to synthetic cosmological galaxy samples. We use catalogues derived from the set of 300 N-body simulations Minerva (Grieb et al. 2016; Lippich et al. 2019). These simulations represent independent realizations of the same cosmology, corresponding to the best-fitting flat Λ CDM model from the WMAP+BOSS DR9 analysis of Sánchez et al. (2013). They are characterized by a total matter and baryon densities $\Omega_{\text{m}} = 0.285$

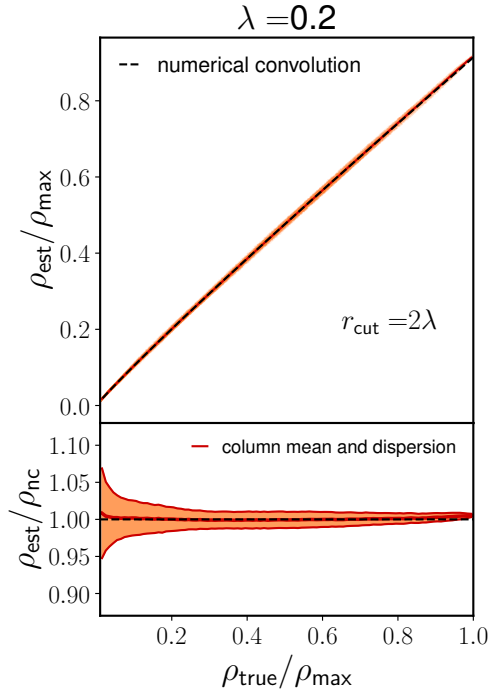


Figure 9. Upper panel: estimated densities for the same spherical point distribution of Section 3.1 plotted against their true values. The densities are estimated using the Gaussian kernel of equation (26) with a smoothing length $\lambda = 0.2$ and truncated at a radius $r_{\text{cut}} = 2\lambda$ and closely follow the convolution of the true density profile with the same kernel, indicated by a black dashed line. Lower panel: the ratios of the estimated densities and their expected values. The red lines indicate the column mean and corresponding dispersion.

and $\Omega_b = 0.046$, a Hubble constant of $H_0 = 69.5 \text{ km s}^{-1} \text{ Mpc}^{-1}$, a scalar spectral index $n_s = 0.968$, and a linear-theory rms mass fluctuation in spheres of radius 12 Mpc, $\sigma_{12} = 0.805$ (Sanchez 2020). The evolution of the dark matter density field was simulated with 1000^3 dark matter particles per realization in a cubic box of side length $L = 1.5h^{-1} \text{ Gpc}$ with periodic boundary conditions. Halos were identified with a standard Friends-of-Friends (FoF) algorithm. To create a synthetic galaxy catalogue, the halos of the snapshot at $z = 0.57$ were populated using the halo occupation distribution (HOD) parametrization of Zheng et al. (2007). This redshift corresponds to the mean redshift of the CMASS sample of BOSS and Grieb et al. (2016) chose the HOD parameters such that the monopole of the mean correlation function from the resulting sample matches the one measured from the CMASS galaxies.

As a first step, we estimated the number density, n_{est} , at the position of each galaxy by smoothing the distribution with a Gaussian kernel as described in Section 4. We used a smoothing length corresponding to the mean interparticle separation, $\lambda = 19.7 \text{ Mpc}$, close to what was found to be the optimal smoothing length for BAO reconstruction in the final BOSS analyses (Alam et al. 2017b). This smoothing length is sufficiently large to avoid discreteness effects, but without erasing too much information on small scales. The truncation radius of the kernel was set to $r_{\text{cut}} = 3\lambda$, which gives the highest signal-to-noise. The density contrast at the position of each galaxy was obtained as $\delta = n_{\text{est}}/\bar{n} - 1$, where \bar{n} is the mean number density.

We computed the MFs on 35 density thresholds equispaced in logarithmic scale around the mean density contrast $\delta = 0$. Fig. 11

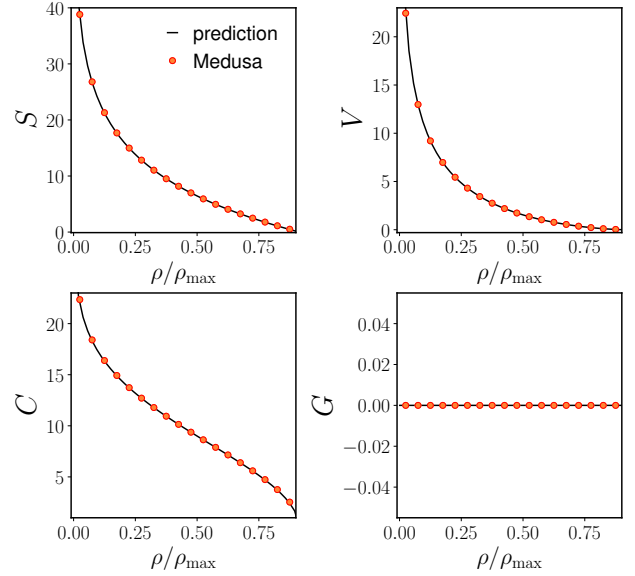


Figure 10. MFs of the same spherical point distribution of Section 3.1 but inferred from density estimates based on a Gaussian kernel with a smoothing length $\lambda = 0.2$ and truncated at a radius $r_{\text{cut}} = 2\lambda$, expressed as a function of the normalized density ρ/ρ_{max} . The black lines shows the theoretical predictions corresponding to the convolved density profile.

shows a section of the isodensity surface corresponding to the threshold $\delta_{\text{th}} = 0.584$ viewed from three different angles. This sample is sparser than the test samples of Section 3, which makes the triangles contributing to the surface more visible than for the toroidal profiles of Fig. 6. This structure has a hole in the center that is visible in panel c), and can then be described by a local genus of 1.

Fig. 12 shows the mean global Minkowski functionals from the 300 Minerva realizations as a function of δ_{th} . In logarithmic scale, the shape of the MFs resembles that of the Gaussian predictions from Fig. 8, but the genus is clearly not symmetric and exhibits different depths for the two minima.

In order to compare MF measurements to theory predictions, the MF densities are typically expressed as functions of the volume-filling fraction f_V . The advantage of this is that the MF densities are expected to be invariant under any local monotonic transformation, if the threshold is adjusted such that that it gives the same volume-filling fraction (Codis et al. 2013). Fig. 13 shows the measured mean Minkowski functional densities and the corresponding Gaussian predictions as a function of f_V . The Gaussian predictions are obtained from equations (21)-(25) using the measured mean galaxy power spectrum multiplied by the Fourier transform of the smoothing kernel. There are clear differences between the measurements and the Gaussian predictions. In particular, the asymmetry of the genus is also obvious here, with the Gaussian prediction providing a better match to the measurement at low f_V values. The measured power spectrum, which is well in the non-linear regime, is dominated by the high-density regions. Hence, it is to be expected that the Gaussian prediction derived from it is in better agreement with the measurements at the high-density end, which corresponds to low f_V values.

It is clear that the Gaussian model cannot be used to analyse

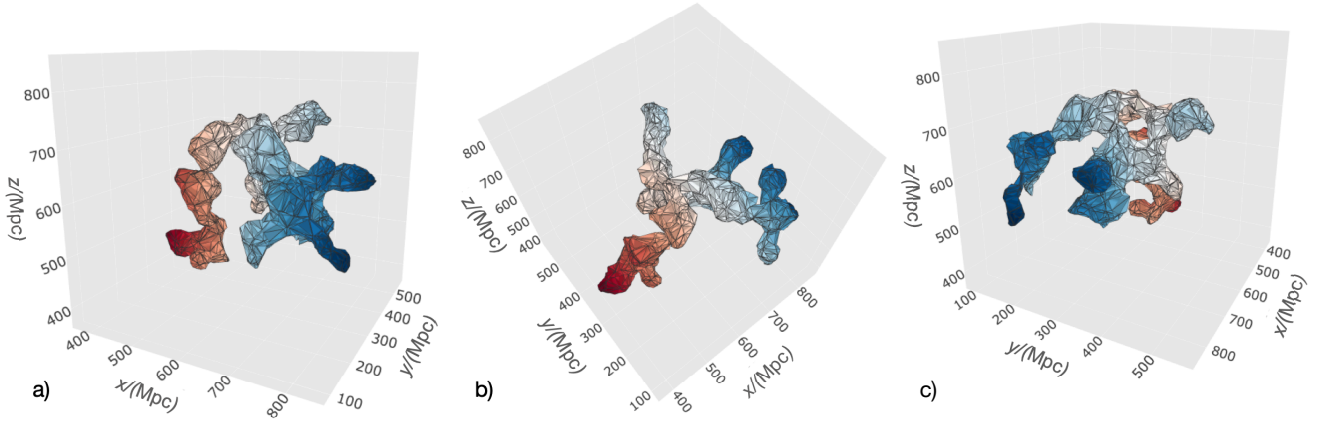


Figure 11. Isosurface of one structure found in the first Minerva HOD galaxy catalogue at a density threshold of $\delta = 0.584$.

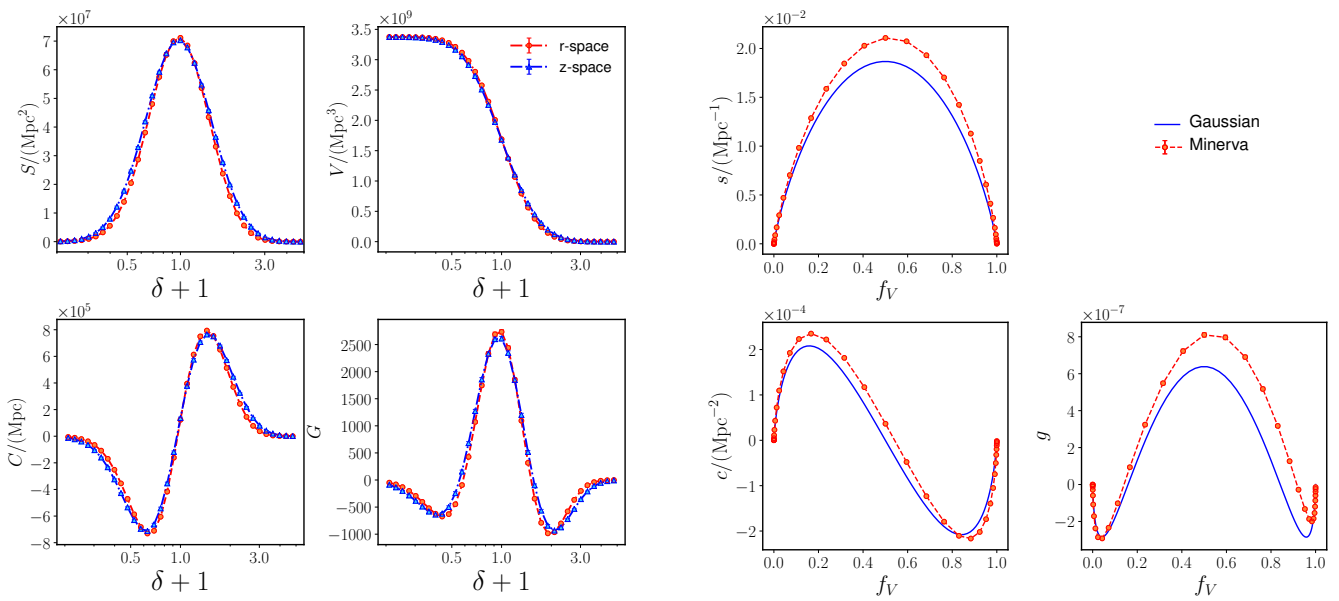


Figure 12. Mean MFs of the 300 Minerva HOD catalogues as a function of the density contrast δ for the real- and redshift-space galaxy density fields (orange and blue, respectively). The error bars corresponding to the standard deviation from the 300 realizations are of the size of the points or smaller and therefore not visible. The densities were estimated with a smoothing length λ corresponding to the mean interparticle separation and a truncation radius $r_{\text{cut}} = 3\lambda$.

the MFs of galaxy catalogues with comparable number density and redshift as our HOD sample. Since the measurements of the surface area, curvature and, in particular, the genus are sensitive to the non-Gaussian features of the density field, they contain complementary information to that of the galaxy power spectrum. We will explore the cosmological information content of these measurements in detail in upcoming work. In the next sections, we will focus on two important observational effects that must be taken into account before measuring the MFs of a real galaxy survey, namely RSD and AP distortions.

Figure 13. MF densities for the mean of the 300 Minerva HOD catalogues measured from the same smoothed galaxy density field in real space as in Fig. 12, but plotted as a function of the volume-filling fraction f_V .

5.2 The effect of redshift-space distortions

To study the effect of RSD on the MFs, we distorted the positions of the HOD galaxies by taking into account the component of their peculiar velocities along one Cartesian axis of the box, which was treated as the line-of-sight direction. Since the total volume and number density are not altered by RSD, we used the same smoothing length as in Section 5.1 to estimate the densities at the distorted galaxy positions. Fig. 12 compares the measurements of the MFs in real and redshift space. The amplitudes of both sets of measurements are very similar, but the redshift-space MFs appear to be stretched towards lower and higher densities than $\delta = 0$ compared to the corresponding ones in real-space.

Fig. 14 shows the same measurements from Fig. 12, but plotted as functions of the volume-filling fraction, f_V . Expressed in this way, the agreement between the MFs in real and redshift space is significantly improved, with only small deviations in their am-

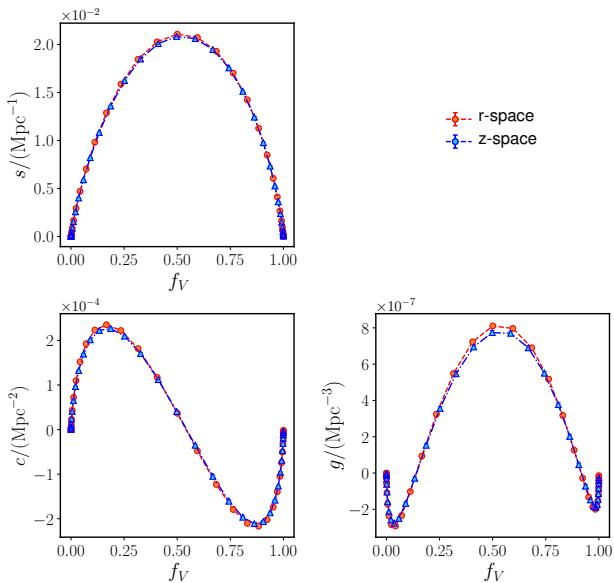


Figure 14. MF densities for the mean of the 300 Minerva HOD catalogues measured from the same smoothed galaxy density field in real and redshift space as in Fig. 12, but plotted as a function of the volume-filling fraction f_V .

plitude. The surface measurements agree at a 2% level, while the deviations in the curvature and genus are smaller than 5% (except for the density thresholds where these MFs are close to zero). RSD do not correspond to a monotonic transformation of the density field. Nonetheless, on average, the mapping from the real-space density threshold, δ_{rs} , to the corresponding value in redshift space, $\delta_{zs}(\delta_{rs})$, can be well described by matching the values of f_V in the two spaces (although the scatter for the individual densities is large). For this reason, the global effect of RSD on the MFs of the Minerva HOD galaxy catalogues is small when these are expressed as functions of f_V . However, this result cannot be generalised to other samples with different number densities or mean redshifts without careful study.

The fact that RSD have only a small effect on the MF densities when expressed in terms of f_V implies that it should be possible to probe the impact of deviations from Gaussianity or the sensitivity to the underlying cosmology without a detailed characterization of the mapping between real and redshift space. However, an accurate modelling of such mapping would open up the possibility to use the measurements of all four MFs and to extract constraints on the growth-rate of cosmic structure. We leave such analysis for a future study.

5.3 The effect of Alcock-Paczynski distortions

The MFs measured from a real galaxy survey will depend on the fiducial cosmology assumed to transform the observed redshifts into comoving distances. Any difference between this cosmology and the true underlying one gives rise to AP distortions (Alcock & Paczynski 1979). The modelling of AP distortions is standard in the analysis of two-point statistics, but has mostly been ignored for MFs. We mimic the effect of AP distortions on our Minerva HOD

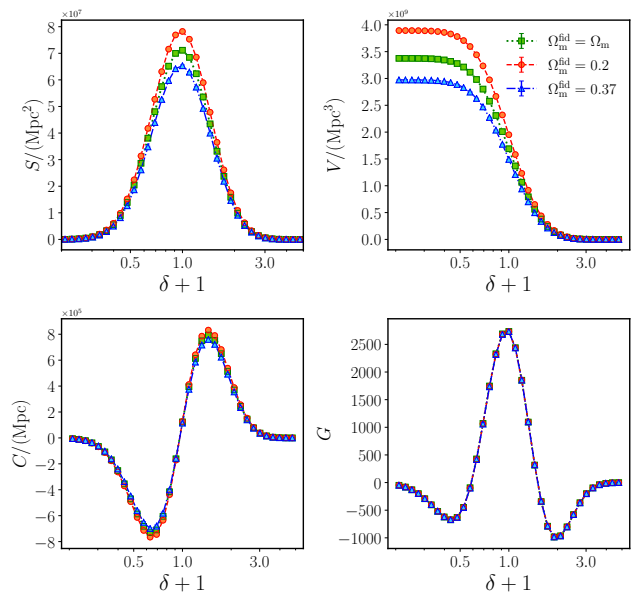


Figure 15. Minkowski Functionals for the mean of the 300 Minerva HOD catalogues as a function of the galaxy density contrast δ for three AP distorted boxes with different fiducial Ω_m^{fid} : a) the undistorted box with $\Omega_m^{\text{fid}} = \Omega_m$, b) $\Omega_m^{\text{fid}} = 0.20$, c) $\Omega_m^{\text{fid}} = 0.37$. The densities are estimated with a kernel of a smoothing length λ corresponding to specific the interparticle and a truncation radius $r_{\text{cut}} = 3\lambda$.

samples by distorting the galaxy positions by

$$x'_{\perp} = \frac{D'_M(z)}{D_M(z)} x_{\perp} \equiv q_{\perp}^{-1} x_{\perp}, \quad (27)$$

for the two Cartesian axes perpendicular to the line of sight and

$$x'_{\parallel} = \frac{H(z)}{H'(z)} x_{\parallel} \equiv q_{\parallel}^{-1} x_{\parallel}, \quad (28)$$

for the line-of-sight coordinate. We computed the values of the comoving angular-diameter distance, $D_M(z)$, and the Hubble parameter $H(z)$ using the true underlying matter density of the Minerva simulations and the fiducial values, $D'_M(z)$ and $H'(z)$, using two different fiducial matter densities $\Omega_m^{\text{fid}} = 0.20$ and $\Omega_m^{\text{fid}} = 0.37$. We applied the same smoothing procedure as in Section 5.1 to the AP distorted HOD galaxy samples, where we again set the smoothing scale λ as the mean inter-particle separation and $r_{\text{cut}} = 3\lambda$. As the volumes of the AP distorted boxes change with respect to the undistorted reference one, also the mean interparticle separations, and therefore the corresponding values of λ and r_{cut} , are adjusted accordingly.

We used MEDUSA to measure the MFs of the resulting density fields using the same density thresholds as in Section 5.1. Fig. 15 shows the mean global MFs as function of the density contrast δ of the original boxes (green points) and the two distorted cases (orange and blue points). There are obvious differences in the amplitudes of S , V , and C for the three different choices of fiducial matter densities. As the topology of the galaxy density field is not changed by the coordinate transformations of equations (27) and (28) the genus is the same in all cases.

As MFs are angle-averaged measurements, they are sensitive to the isotropic AP parameter,

$$q = \left(q_{\perp}^2 q_{\parallel} \right)^{1/3} = \frac{D_V(z)}{D'_V(z)}, \quad (29)$$

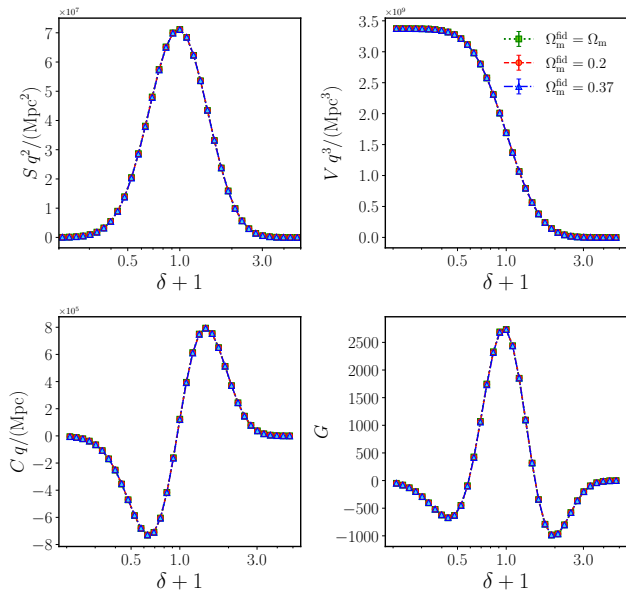


Figure 16. The same as Fig. 15, but now the MFs are normalized by the corresponding powers of the isotropic AP parameter q .

which depends on the volume-averaged distance

$$D_V(z) = \left(D_M(z)^2 c z / H(z) \right)^{1/3}. \quad (30)$$

The coordinate transformation associated with AP distortions is described by the Jacobian of the volume and surface integrals of the MFs. Following from this, the global MFs transform under AP distortions as

$$S = q^2 S', \quad (31)$$

$$V = q^3 V', \quad (32)$$

$$C = q C', \quad (33)$$

while the genus remains unaffected. Equivalently, the AP distorted MF densities can be rescaled by the factors q^α , with $\alpha = 0, -1, -2, -3$ for $f_V', s', c',$ and g' to obtain the undistorted MF densities. Fig. 16 shows the global MFs rescaled by the corresponding powers of q , which are in excellent agreement with the undistorted reference measurements.

The correction factors of equations (31) – (33) must be taken into account before any model of the MFs can be compared against measurements inferred from galaxy redshift surveys. They also show that these measurements can be used to constrain q , and hence the volume-averaged distance $D_V(z)$. This was the approach followed by Blake et al. (2014), who used Gaussian theory predictions to derive constraints on $D_V(z)$ from the differential MFs of WiggleZ. As we discussed in Section 5.1, the Gaussian predictions do not give a correct description of the MFs of our HOD catalogues, indicating that the derivation of unbiased constraints on $D_V(z)$ from real galaxy samples with similar clustering properties (such as the BOSS CMASS sample) would require a more accurate treatment of the impact of non-linearities on the MFs.

6 DISCUSSION AND CONCLUSIONS

We presented MEDUSA, an implementation of a robust and accurate method to estimate the MFs of a three-dimensional distri-

bution of points with known densities. Given a density threshold, MEDUSA performs two main steps: First, closed triangulated surfaces are constructed from the tetrahedra of the Delaunay tessellation of the points. This is done by selecting the tetrahedra that contain vertices with densities above and below the threshold. The isodensity surface is then defined by linear interpolation of the densities of those vertices. The second main step is the evaluation of the four MFs, volume, surface area, integrated mean curvature and Euler characteristic, of the triangulated surface by summing over the contributions of all tetrahedra and triangles contributing to it. An earlier implementation of the same basic algorithm was described in Yaryura et al. (2004). We extended previous works on the estimation of MFs on triangulated surfaces by implementing periodic boundary conditions, which are essential for the analysis of N-body simulations. The MFs computed by MEDUSA can be used to study the geometry and topology of the sample being analysed.

We tested MEDUSA by applying it to estimating the MFs of test samples with different geometrical and topological properties. We considered spherical, ellipsoidal and toroidal density distributions for which theoretical predictions of the MFs can be computed. In all cases, the estimated volume, surface area and extrinsic curvature agree significantly better than one per-cent with the theoretical predictions. The Euler characteristic, which is directly related to the genus, is computed exactly. We also estimated the MFs of different spherical distributions intersecting the edges of a box with periodic boundary conditions and found the same level of agreement with the theoretical predictions. As a further test sample, we used 100 GRFs with periodic boundary conditions, for which there are known analytical predictions of the MFs that are sensitive to the power spectrum of the sample. We found a good agreement between the results of MEDUSA and the theoretical predictions.

After validating the performance of MEDUSA against test samples with known underlying density distributions, we applied it to the analysis of 300 HOD galaxy catalogues from our Λ CDM Minerva simulations at $z = 0.57$. As a first step, we estimated the densities associated with every point in the sample by means of a Gaussian kernel with a fixed smoothing length matching the mean inter-particle separation of the sample. We studied the MFs of the HOD catalogues as a function of the density contrast δ and the volume-filling fraction f_V . Three important aspects must be taken into account before measurements of the MFs of real galaxy redshift surveys can be used as cosmological probes: non-Gaussian signatures due to non-linear gravitational evolution, RSD, and AP distortions. Our main conclusions on these topics are:

(i) The measured MFs are sensitive to deviations from a Gaussian distribution. In particular the asymmetry of the genus is an interesting non-Gaussian signal. Since the MFs encode information from high-order statistics, they are promising tools to study the non-linear galaxy density field as complementary probes to the standard two-point analyses.

(ii) The full measurements of the MFs are affected by RSD. An accurate model of the mapping between the real- and redshift-space densities would make it possible to extract information on the growth rate of cosmic structure from these measurements. However, when expressed as a function f_V , the impact of RSD on the MFs of our HOD samples is greatly reduced. This opens up the possibility to probe deviations from Gaussianity using redshift-space measurements even without a detailed modelling of RSD.

(iii) The volume, surface area, and curvature are sensitive to AP distortions. The topology of the density field is not affected by AP distortions, and hence the Euler characteristic and genus are

independent of the fiducial cosmology. The impact of AP distortions on the MFs can be accounted for by rescaling the theory predictions by the corresponding powers of the isotropic AP parameter q . This parameter is directly related to the volume-averaged distance $D_V(z)$, which can therefore be constrained from these measurements.

In forthcoming studies, we aim to analyse in detail the sensitivity of the MFs to specific cosmological parameters and to explore the cosmological implications of MFs measurements inferred from real galaxy surveys. This will require implementing and testing a description of the MFs of the non-linear galaxy density field. The recently published analytic expressions for the MFs up to second-order corrections in non-Gaussianity by Matsubara & Kuriki (2020) and the modelling of RSD by Codis et al. (2013) will be of great help. Our final goal is to advance the analysis of MFs as a powerful complement of the standard two-point clustering statistics.

ACKNOWLEDGEMENTS

ML and AGS thank Daniel Farrow, Jiamin Hou, Andrea Pezzotta and Agne Semenaite for their help and useful discussions.

The MEDUSA measurements and analyses presented here have been performed on the high-performance computing resources of the Max Planck Computing and Data Facility (MPCDF) in Garching.

The plots of the 3D isodensity surfaces have been created with the free version of the Python graphing library Plotly (Plotly Technologies Inc. 2015).

DATA AVAILABILITY

The data underlying this article will be shared on reasonable request to the corresponding authors.

REFERENCES

- Alam S., et al., 2017a, *MNRAS*, **470**, 2617
 Alam S., et al., 2017b, *MNRAS*, **470**, 2617
 Alcock C., Paczynski B., 1979, *Nature*, **281**, 358
 Appleby S., Park C., Hong S. E., Hwang H. S., Kim J., 2020, *ApJ*, **896**, 145
 Aragon-Calvo M. A., Shandarin S. F., Szalay A., 2010, in 2010 International Symposium on Voronoi Diagrams in Science and Engineering. IEEE Computer Society, Los Alamitos, CA, USA, pp 235–243, doi:10.1109/ISVD.2010.33, <https://doi.ieeecomputersociety.org/10.1109/ISVD.2010.33>
 Blake C., et al., 2011, *MNRAS*, **418**, 1707
 Blake C., James J. B., Poole G. B., 2014, *MNRAS*, **437**, 2488
 Buchert T., France M. J., Steiner F., 2017, *Classical and Quantum Gravity*, **34**, 094002
 Chen Z., Xu Y., Wang Y., Chen X., 2019, *ApJ*, **885**, 23
 Choi Y.-Y., Park C., Kim J., Gott J. Richard I., Weinberg D. H., Vogeley M. S., Kim S. S., SDSS Collaboration 2010, *ApJS*, **190**, 181
 Codis S., Pichon C., Pogosyan D., Bernardeau F., Matsubara T., 2013, *MNRAS*, **435**, 531
 Cole S., et al., 2005, *MNRAS*, **362**, 505
 DESI Collaboration et al., 2016, arXiv e-prints, p. arXiv:1611.00036
 Davis M., Peebles P. J. E., 1983, *ApJ*, **267**, 465
 Drinkwater M. J., et al., 2010, *MNRAS*, **401**, 1429
 Efstathiou G., et al., 2002, *MNRAS*, **330**, L29
 Eisenstein D. J., et al., 2005, *ApJ*, **633**, 560
 Gay C., Pichon C., Pogosyan D., 2012, *Phys. Rev. D*, **85**, 023011
 Gil-Marín H., et al., 2015, *MNRAS*, **452**, 1914
 Gil-Marín H., Percival W. J., Verde L., Brownstein J. R., Chuang C.-H., Kitaura F.-S., Rodríguez-Torres S. A., Olmstead M. D., 2017, *MNRAS*, **465**, 1757
 Gott J. Richard I., Melott A. L., Dickinson M., 1986, *ApJ*, **306**, 341
 Gott J. R., Choi Y.-Y., Park C., Kim J., 2009, *ApJ*, **695**, L45
 Grieb J. N., Sánchez A. G., Salazar-Albornoz S., Dalla Vecchia C., 2016, *MNRAS*, **457**, 1577
 Hikage C., et al., 2003, *PASJ*, **55**, 911
 Hikage C., Komatsu E., Matsubara T., 2006, *ApJ*, **653**, 11
 James J. B., Colless M., Lewis G. F., Peacock J. A., 2009, *MNRAS*, **394**, 454
 Kerscher M., 2000, in Statistical physics and spatial statistics: The art of analyzing and modeling spatial structures and pattern formation, ed. K. R. Mecke & D. Stoyan, Lecture notes in physics, No. 554 (Berlin: Springer Verlag)
 Kerscher M., et al., 1997, *MNRAS*, **284**, 73
 Kerscher M., Schmalzing J., Buchert T., Wagner H., 1998, *A&A*, **333**, 1
 Kerscher M., et al., 2001, *A&A*, **377**, 1
 Laureijs R., et al., 2011, preprint, (arXiv:1110.3193)
 Lippich M., et al., 2019, *MNRAS*, **482**, 1786
 Liu Y., Yu Y., Yu H.-R., Zhang P., 2020, arXiv e-prints, p. arXiv:2002.08846
 Marín F. A., et al., 2013, *MNRAS*, **432**, 2654
 Matsubara T., 1994, *ApJ*, **434**, L43
 Matsubara T., 2003, *ApJ*, **584**, 1
 Matsubara T., 2010, *Phys. Rev. D*, **81**, 083505
 Matsubara T., Kuriki S., 2020, arXiv e-prints, p. arXiv:2011.04954
 Matsubara T., Hikage C., Kuriki S., 2020, arXiv e-prints, p. arXiv:2012.00203
 Mecke K. R., Buchert T., Wagner H., 1994, *A&A*, **288**, 697
 Munshi D., Namikawa T., McEwen J. D., Kitching T. D., Bouchet F. R., 2020, arXiv e-prints, p. arXiv:2010.05669
 Park C., et al., 2005, *ApJ*, **633**, 11
 Parroni C., Cardone V. F., Maoli R., Scaramella R., 2020, *A&A*, **633**, A71
 Pearson D. W., Samushia L., 2018, *MNRAS*, **478**, 4500
 Peebles P. J. E., 1993, Principles of Physical Cosmology. Princeton University Press
 Perez L. A., Malhotra S., Rhoads J. E., Tilvi V., 2020, arXiv e-prints, p. arXiv:2011.03556
 Petri A., Haiman Z., Hui L., May M., Kratochvil J. M., 2013, *Phys. Rev. D*, **88**, 123002
 Planck Collaboration et al., 2020, *A&A*, **641**, A7
 Plotly Technologies Inc. 2015, Collaborative data science, <https://plot.ly>
 Pogosyan D., Gay C., Pichon C., 2009, *Phys. Rev. D*, **80**, 081301
 Repp A., Szapudi I., 2020, *MNRAS*, **498**, L125
 Sanchez A. G., 2020, arXiv e-prints, p. arXiv:2002.07829
 Sánchez A. G., Baugh C. M., Percival W. J., Peacock J. A., Padilla N. D., Cole S., Frenk C. S., Norberg P., 2006, *MNRAS*, **366**, 189
 Sánchez A. G., et al., 2013, *MNRAS*, **433**, 1202
 Sánchez A. G., et al., 2017, *MNRAS*, **464**, 1640
 Schaap W. E., van de Weygaert R., 2000, *A&A*, **363**, L29
 Schmalzing J., Buchert T., 1997, *ApJ*, **482**, L1
 Schmalzing J., Gorski K. M., 1998, *MNRAS*, **297**, 355
 Schmalzing J., Kerscher M., Buchert T., 1996, in Bonometto S., Primack J. R., Provenzale A., eds, Dark Matter in the Universe. p. 281 (arXiv:astro-ph/9508154)
 Schmalzing J., Gottlöber S., Klypin A. A., Kravtsov A. V., 1999a, *MNRAS*, **309**, 1007
 Schmalzing J., Buchert T., Melott A. L., Sahni V., Sathyaprakash B. S., Shandarin S. F., 1999b, *ApJ*, **526**, 568
 Sheth J. V., 2004, *MNRAS*, **354**, 332
 Sheth J. V., Sahni V., Shandarin S. F., Sathyaprakash B. S., 2003, *MNRAS*, **343**, 22
 Slepian Z., et al., 2017a, *MNRAS*, **468**, 1070
 Slepian Z., et al., 2017b, *MNRAS*, **469**, 1738
 Spurio Mancini A., Taylor P. L., Reischke R., Kitching T., Pettorino V., Schäfer B. M., Zieser B., Merkel P. M., 2018, *Phys. Rev. D*, **98**, 103507
 Tegmark M., et al., 2004, *ApJ*, **606**, 702

- Tomita H., 1990, in *Formation, Dynamics, and Statistics of Patterns* (Kawasaki, K., Suzuki, M., & Onuki, A., eds.), Vol. 1, World Scientific, pp 113–157
- Uhlemann C., Friedrich O., Villaescusa-Navarro F., Banerjee A., Codis S. r., 2020, *MNRAS*, **495**, 4006
- Wang Y., Park C., Xu Y., Chen X., Kim J., 2015, *ApJ*, **814**, 6
- Weinberg D. H., Gott III J. R., Melott A. L., 1987, *ApJ*, **321**, 2
- White S. D. M., 1979, *MNRAS*, **186**, 145
- Wiegand A., Eisenstein D. J., 2017, *MNRAS*, **467**, 3361
- Wiegand A., Buchert T., Ostermann M., 2014, *MNRAS*, **443**, 241
- Yaryura C. Y., Sánchez A. G., García Lambas D., 2004, *Boletín de la Asociación Argentina de Astronomía La Plata Argentina*, **47**, 377
- Yoshiura S., Shimabukuro H., Takahashi K., Matsubara T., 2017, *MNRAS*, **465**, 394
- Zhang Y., Springel V., Yang X., 2010, *ApJ*, **722**, 812
- Zheng Z., Coil A. L., Zehavi I., 2007, *ApJ*, **667**, 760
- de Lapparent V., Geller M. J., Huchra J. P., 1991, *ApJ*, **369**, 273
- eBOSS Collaboration et al., 2020, arXiv e-prints, p. [arXiv:2007.08991](https://arxiv.org/abs/2007.08991)

This paper has been typeset from a \TeX/L\AA\TeX file prepared by the author.